Available online at www.sciencedirect.com
ScienceDirect
Trans. Nonferrous Met. Soc. China 34(2024) 1347−1364
Transactions of Nonferrous Metals Society of China
www.tnmsc.cn

Mechanism of catalyst on morphological evolution of $Al(OH)_3$ during $Al-H_2O$ reaction

Wen-qi TANG[1], Ji-yi ZHU[1], Hui SUN[2], Yong-fei JUAN[1], Chao-peng FU[1], Jian YANG[1], Jiao ZHANG[1,3]

1. State Key Lab of Metal Matrix Composites, School of Materials Science and Engineering, Shanghai Jiao Tong University, Shanghai 200240, China;
2. School of Mechanical Engineering, Shanghai Dianji University, Shanghai 201306, China;
3. Collaborative Innovation Center for Advanced Ship and Deep-sea Exploration, Shanghai Jiao Tong University, Shanghai 200240, China

Received 19 November 2022; accepted 20 July 2023

Abstract: The morphologies of $Al(OH)_3$ crystals prepared via the $Al-H_2O$ reactions with various catalysts and the growth mechanisms of these crystals were investigated. The reaction was carried out with NaOH, KOH, tetramethylguanidine (TMG), and tetramethylammonium hydroxide (TMAH) as catalysts. The evolution of the obtained product was observed in situ, and the products obtained after 120 min of reaction have the shapes of the hexagonal prism, long-hexagonal prism, long rod, and irregular rod, respectively. In the NaOH and KOH systems, the products are gibbsite, and the gibbsite crystals grow along the (110), (001), and (100) faces in the NaOH system, and the (100), (102), and (110) faces in the KOH system. However, in the TMG and TMAH systems, the products are bayerite, and the bayerite crystals grow along the (110), (111), and (001) faces. It is worth mentioning that gibbsite has more Al—O bonds than bayerite, giving rise to the formation of columnar crystals.

Key words: crystal growth; aluminum hydroxide; preferential orientation coefficient; aluminum−water reaction; in situ observation

1 Introduction

$Al(OH)_3$ is widely used in flame retardants, rubber, building materials, coatings, pharmaceuticals, and other fields [1−3], especially as a precursor of alumina [4,5], and the properties of alumina generally inherit the precursor [6,7]. To date, the properties of $Al(OH)_3$ can be modified by manipulating the $Al-H_2O$ reaction, because no impurities are introduced and only hydrogen is produced during the whole reaction [8,9]. However, these studies were mainly focused on the collection and preparation of hydrogen gas, and the $Al(OH)_3$ is ignored [10]. The $Al-H_2O$ reaction eliminates the alumina film on the aluminum surface, triggering a reaction between water and aluminum, which produces the hydrogen gas and the aluminum hydroxide [11,12].

Generally, the morphology of the $Al(OH)_3$ depends on the preparation methods [13]. The reaction of aluminum nanoparticles with water can produce hourglass-like particles of bayerite [14], and the reaction of aluminum with hot water (95 °C) can form bayerite nanorods and boehmite fibers [15,16]. Aluminum is hydrolyzed at 100 °C and through sol−gel treatment can produce fibrous boehmite [17], and aluminum powder reacts with supercritical water to produce alumina nanoparticles [18]. The bayerite particles are

Corresponding author: Jian YANG, Tel: +86-18817553561, E-mail: tracyang@sjtu.edu.cn;
Jiao ZHANG, Tel: +86-21-34202952, E-mail: zj119@sjtu.edu.cn
DOI: 10.1016/S1003-6326(24)66476-9

initially formed as prismatic particles with serrated edges in the Al−H_2O reaction and subsequently agglomerate into hourglass shapes [19]. In addition, aluminum powder reacts with water during ball milling, producing nano spindle and nano rod-like $Al(OH)_3$ after 7 and 12 h of grinding at room temperature, respectively [20]. Studying the mechanisms of $Al(OH)_3$ crystal growth is essential for preparing specific morphologies, which can effectively broaden its application and meet the needs of alumina preparation in backend processes. Although a few reports exist on the evolution mechanism of the $Al(OH)_3$ morphology during the Al−H_2O reaction, more research work has been done in other fields, specifically on gibbsite and bayerite.

The gibbsite structure consists of two layers of OH^- ions stacked along the [001] axis. Hydrogen bonds hold the layers together, and the Al ions occupy two-thirds of the octahedral interstices in the anionic layer. This structure leads to the basal plane consisting of two hexagonal arrangements [21]. In the crystal growth of gibbsite, (001), (100), and (010) faces essentially grow as plate-like crystals, and (110), (101), and (112) faces tend to grow as more elongated rod-like crystals [22,23]. Moreover, the previous simulation studies have shown that the face energy of the gibbsite crystal is $E_{sur}(011) > E_{sur}(100) > E_{sur}(110) > E_{sur}(001)$ [24]. The (100) face is more energetically unstable compared to the (001) and (110) faces, so the equilibrium morphology of the gibbsite tends to consist of two (001) faces and four (110) sides [25]. The gibbsite crystals are formed by the aggregation of tiny hexagonal prisms and multifaceted rhombuses, and hexagonal crystals develop into large lamellae, further growing into large prismatic crystals with chamfered faces [26].

Bayerite is less found in nature and usually prepared by hydrolysis and neutralization [27−29]. The bayerite prepared by these methods has a large particle size and various shapes, including conical, prismatic, wedge-shaped, rod-shaped, and hourglass-shaped [30]. The crystallite size and morphology of bayerite vary depending on the preparation conditions. The pH value and sodium aluminate solution concentration can affect the size and morphology of bayerite. Furthermore, rod-shaped and flat-shaped bayerites can be obtained at high and low pH values, respectively [31]. Therefore, crystals with rod, conical, and ovoid can be prepared by adjusting the growth parameters [32,33].

In addition, the alkali ions (K^+, Na^+) in the alkaline solution can affect the crystal morphology of $Al(OH)_3$ but have little influence on its twinning behavior. The difference in the morphology of the precipitates may be limited by the alkaline system [34−36]. Generally, the pH value in the solution after the reaction is commonly inconsistent and may result in a difference in morphology [37]. Likewise, the concentration of aluminate ions also influences the formation process and the morphology of gibbsite and bayerite. Modifying the concentration of aluminate ions implies increasing or decreasing driving force and base concentration, leading to a rapid morphological evolution of gibbsite and bayerite. Larger crystals are obtained at higher driving forces and concentrations of aluminate [26,38,39]. The synthesis of products in supersaturated aluminate solutions implies that the crystallographic structure does not affect the group structure [40].

The growth of gibbsite and bayerite crystals is influenced by temperature and supersaturation. At a higher temperature (120 °C), a facile hydrothermal method can be used to synthesize gibbsite nanorods with a high aspect ratio [41]. At a lower temperature (50 °C), the gibbsite crystals grow preferentially along [100] direction, resulting in the formation of hexagonal shapes and aggregation to form larger particles [25,42]. Bayerite crystals are predominantly ovoid at 90 °C and exhibit increased particle size due to agglomeration. Bayerite crystals are mainly pyramidal and conical at low temperatures (50 °C), and the nucleation rate of particles exceeds the growth and agglomeration rate [30,43]. In both low- and high-supersaturated solutions, not only rhombic and hexagonal gibbsite crystals are formed, but other shapes are also observed. In some cases, these crystals deviate from the perfect rhombic or hexagonal crystals. As the degree of supersaturation increases, hexagonal lamellar gibbsite crystals are formed. The number of sheets, prisms, and hexagons gibbsite depends on the degree of supersaturation [44]. Rough side faces are observed in the higher supersaturations, while at lower values, lozenges and truncated lozenges are found [22]. Even small deviations in supersaturation can result in significant differences in the shape and size of bayerite. In highly supersaturated

solutions, the fast nucleation rate is beneficial to forming many small particles [45].

In this study, catalysts including NaOH, KOH, TMG, and TMAH were employed to investigate mechanism during Al−H_2O reaction. Observations were made in situ on the generation of bubbles and the evolution of crystals. The growth mechanism of $Al(OH)_3$ crystals was analyzed by calculating the preferential orientation coefficient and crystallite size.

2 Experimental

2.1 Materials and methods

200 mL of ultrapure water (with Resistivity $>10^5$ Ω·cm) was put into the automatic parallel reactor, and 5.19 g of NaOH, 7.27 g of KOH, 14.93 g of TMG, and 11.82 g of TMAH (molar ratio of catalyst to aluminum powder is 1:2) were added to the automatic parallel reactor, respectively. Then, 7 g of aluminum powder (with Al content >99.99%) was added when the solution temperature reached 85 °C. And the focused beam reflectometer was inserted simultaneously into the solution and mechanically stirred at 400 r/min. Subsequently, the reaction proceeded to the end of 120 min to obtain a white slurry, which was filtered and dried to obtain a white precipitate for characterization and analysis.

2.2 Electrochemical testing

Open circuit potential (OCP) and Tafel polarization were measured in NaOH, KOH, TMG, and TAMH solutions, respectively, with a standard three-electrode configuration on the potentiostat (CHI 760E). The mercury/mercury oxide electrode (Hg/HgO) was used as the reference electrode, while a platinum sheet (20 mm × 20 mm) was used as the counter electrode, and aluminum foil (purity >99.99%, 20 mm × 20 mm) was used as the working electrode. Potentiodynamic polarization was measured at a scan rate of 5 mV/s.

2.3 Characterizations

Aluminum powder reacted with ultrapure water in the automatic parallel reactor (APR, Easy Max 402, Mettler Toledo). The reaction in the solution was observed in real-time by the focused beam reflectometer (FBR, Particle Track G400, Mettler Toledo) when inserted into APR, and the reaction process was recorded by taking photos. The phases of the precipitates were examined by X-ray diffraction (XRD, Mini Flex 600, Rigaku) with Cu K_α radiation (λ=0.15418 nm) at a scanning speed of 2 (°)/min. The morphology of the precipitates was measured by scanning electron microscope (SEM, Sirion 209, FEI) with an accelerating voltage of 5 kV. And the morphology, the patterns of selected area electron diffraction (SAED), and the high-resolution transmission electron microscope (HR-TEM) images of the precipitates were measured by field emission transmission electron microscopy (FE-TEM, Talos F200X, FEI) at 200 kV. The functional group of precipitates was analyzed by Fourier transform infrared spectrometer (FTIR, Nicolet 6700, Thermo Fisher). The precipitates and potassium bromide were mixed and ground in an agate mortar at a ratio of 1:10, and then the mixed sample was pressed into a semitranslucent. Moreover, the resolution of the infrared spectrum was 4 cm^{-1} and the range was between 4000 and 400 cm^{-1} with an average of 16 scans. The pH values were measured by pH meter (PM, S220, Mettler), and samples were taken at 5 min intervals. The temperature was measured by a mercury thermometer and recorded at 30 s intervals. Aluminum ions in solution were measured by inductively coupled plasma optical emission spectrometer (ICP-MS, Avio 500, Platinum Elmer).

The crystallite size of gibbsite and bayerite with the corresponding faces was calculated by the Scherrer equation as $D=K\lambda/(\beta\cos\theta)$. λ and θ represent the X-ray wavelength and Bragg angle, respectively. β is the peak width of the diffraction peak profile at the half-maximum height, expressed in radians. The constant K is related to β and set to be 0.89. According to the XRD patterns, the preferential orientation coefficient (T) (or texture coefficient) is calculated as follows:

$$T_{(khl)}=\left(I_{hkl}/I^0_{hkl}\right)\Big/\left(\frac{1}{N}\sum\frac{I_{hkl}}{I^0_{hkl}}\right) \quad (1)$$

where I_{hkl} is the measured intensity of (hkl), and I^0_{hkl} is the theoretical relative intensity of XRD reference data (The JCPDS of gibbsite is No. 70-2038 and that of bayerite is No. 74-1119). N represents the number of crystal faces, and we select nine faces with a higher intensity (I_{hkl}) in the calculation (N=9) [46].

3 Results and discussion

3.1 In situ observation and analysis in solution

The growth and evolution mechanism of $Al(OH)_3$ in $Al-H_2O$ reaction were investigated systematically. The reaction process between aluminum powder and water was monitored synchronously according to the detection information fed back by FBR. Figure 1 shows that the water strongly reacted with aluminum powder at the beginning of the reaction (5 min) to generate many bubbles (hydrogen). The number of bubbles in the four systems decreased at around 30 min as the reaction progressed, indicating that the reaction rate gradually slowed down.

Figure 1(a) shows no bubbles generated after 62 min in the NaOH system. At the same time, quadrilateral-like particles appeared in the solution. Furthermore, the particles gradually aggregated and grew slowly after 75 min. The particles no longer grew after 103 min, and the overall size changed little. The morphology of the particles no longer changed, and they aggregated in the form of small particles at 120 min. In the KOH system, the number of bubbles in the solution decreased and quadrangular particles were generated after 51 min reaction, as shown in Fig. 1(b). There were no bubbles and more quadrangular particles occurred in the solution after 71 min. The particles no longer grew, and most of them aggregated in the form of a long quadrilateral in the solution after 100 min. The morphology of the particles remained unchanged during this time. Similarly, the TMG system also generated new particles after 69 min (Fig. 1(c)). These particles were similar to round bars, and no bubbles were generated in the solution after 81 min. The particles no longer grew, but were distributed in the solution with an irregular rod-like shape after 108 min. A few bubbles and small rod-shaped particles appeared after 73 min in the TMAH system (Fig. 1(d)). Many new particles appeared and no bubbles were generated after 87 min. Subsequently, the particles gradually agglomerated after 98 min, and the particles were irregularly rod-like and distributed in the solution at 120 min.

It is verified by in situ observation that the catalysts act on the surface of Al powder to destroy the alumina film, and then Al begins to react with H_2O to produce bubbles (hydrogen). Further, the reaction degree is evaluated by the generation or disappearance of the bubbles. The disappearance of bubbles in the NaOH, KOH, TMAH, and TMG reaction systems occurs at 62, 51, 69, and 73 min, respectively. By contrast, the KOH system has the fastest reaction rate. However, the hydrogen production rate is independent of the change in particle size, where the particle in the TMAH system has a faster growth rate. It is indicated that the catalysts act on the aluminum surface for hydrogen production and there have differences in the growth of $Al(OH)_3$ particles in different reaction systems.

The reaction system displayed temperature changes, starting with an upward trend, followed by a downward trend, and eventually stabilizing at the same level as water bath temperature (85 °C), as shown in Fig. 2(a). An increase in temperature occurred during the initial stage, for particularly around 10 min, in which the temperature in the solution peaked due to the intense reaction process, which was consistent with FBR observations. The TMG system demonstrated higher temperatures during the reaction, reaching up to a maximum of 94.0 °C at 10 min compared to other systems. These observations illustrate that the $Al-H_2O$ reaction in the solution is more vigorous, and the ability to destroy the aluminum oxide on the surface of the aluminum is stronger than in the other systems. Evidently, $Al-H_2O$ reactions in these exothermic systems generate a significant amount of heat, as the aluminum reacts with water rapidly after destroying the film.

Aluminum is an amphoteric metal that can react with bases or acids. Figure 2(b) displays a gradual increase in the mass ratio of AlO_2^- during the reaction. The mass fractions of AlO_2^- in the NaOH and KOH systems are similar, reaching 0.157% and 0.149% at 120 min, respectively, due to the comparable chemical properties of these two reagents. In contrast, the AlO_2^- content in the TMG and TMAH systems is relatively small, reaching 0.017% and 0.035% at 120 min, respectively. Although a small amount of aluminum reacts with these basic reagents during the reaction, the AlO_2^- content remains below 0.16%, which can be considered to be negligible. Consequently, these catalysts do not participate in the $Al-H_2O$ reaction.

As known, these four basic reagents are capable of ionizing OH^- directly in the solution.

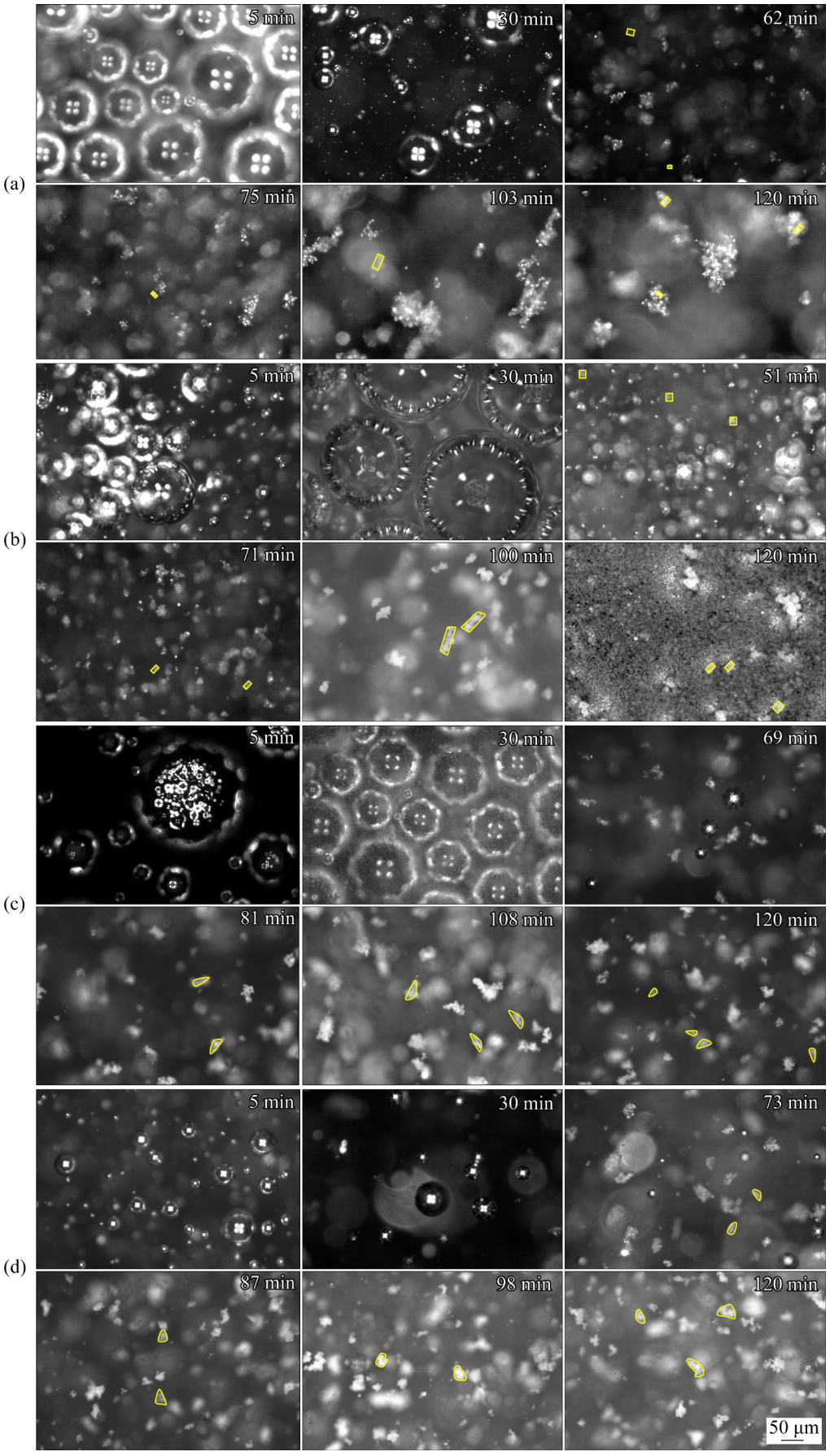

Fig. 1 FBR images of NaOH (a), KOH (b), TMG (c), and TMAH (d) systems during reaction

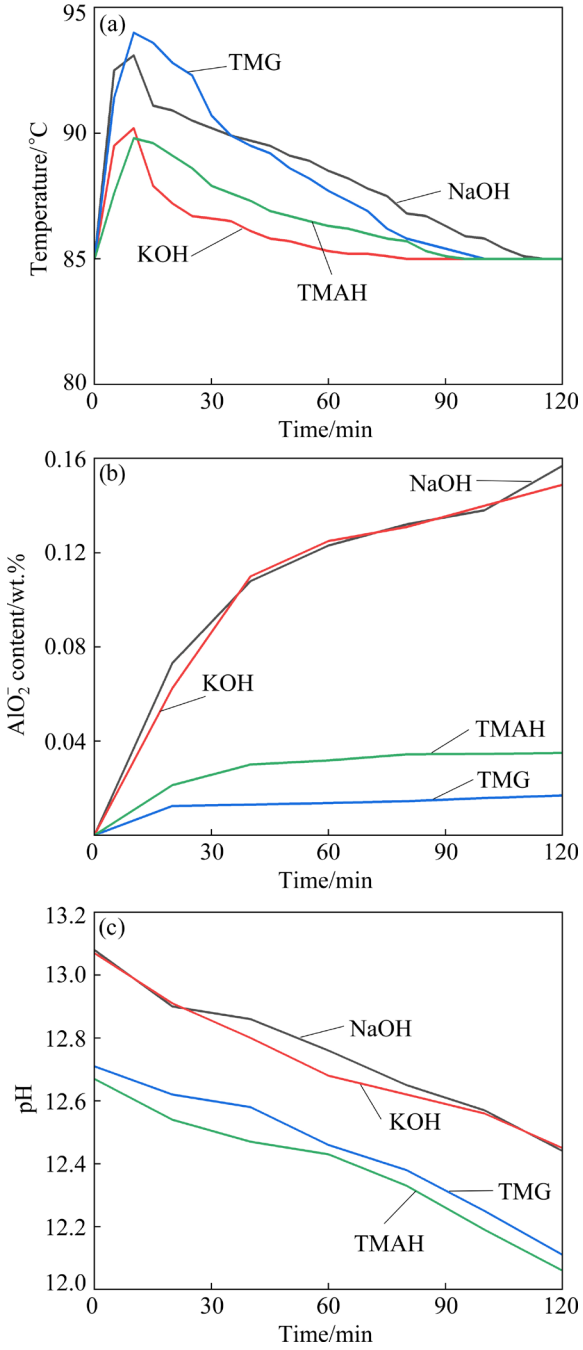

Fig. 2 Temperature (a), content of AlO_2^- (b), and pH (c) in solution during reaction

Therefore, the amount of these reagents present in the solution has a positive correlation with the pH of the solution. The initial pH values in the reactions reveal that NaOH and KOH solutions exhibit stronger alkalinity with a pH of 13.08 and 13.07, respectively. In contrast, the TMG and TMAH solutions have pH values of 12.71 and 12.67, respectively (Fig. 2(c)). As the reaction progresses, the pH of each system decreases and follows a nearly linear trend. This can be attributed to a small amount of reagent reacting with aluminum, which slightly changes the pH values. Furthermore, the pH difference before and after the reaction in each system is within 0.62, suggesting that the four reagents are not consumed much during the reaction and most of them remain in the solution.

3.2 Electrochemical testing results during reaction

High-purity aluminum foil was used as the working electrode for electrochemical testing, which can obtain the electrochemical properties of the foil in different systems and analyze the reaction rate of the catalyst acting on the aluminum. Figure 3(a) shows the Tafel plots of the aluminum foil in different systems, and the extracted electrochemical parameters are listed in Table 1. Aluminum foil has the most negative self-corrosion potential and the smallest self-corrosion current density in the TMAH system, and the corrosion current density in the reaction is only 4.82 mA/cm^2.

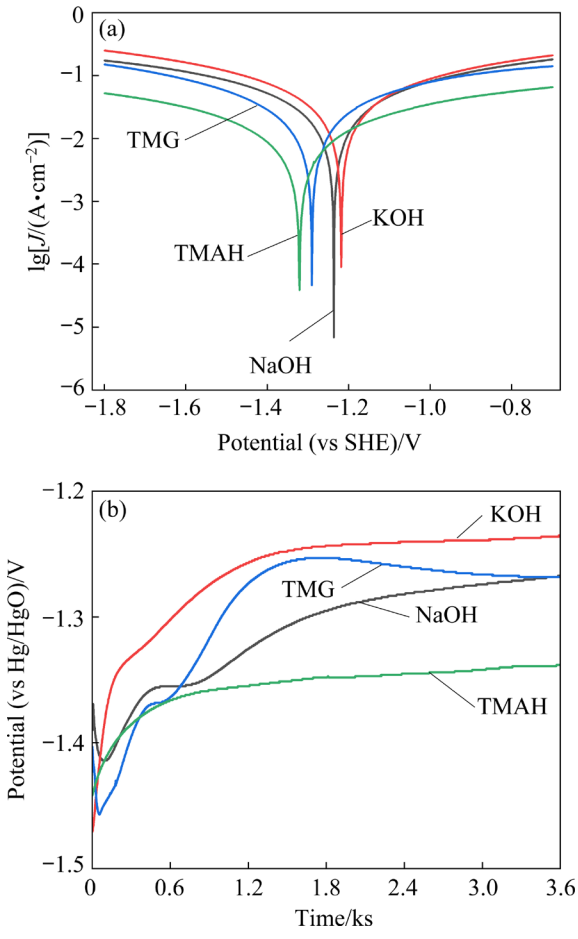

Fig. 3 Electrochemical behavior of aluminum foil during reaction of different systems: (a) Tafel plots; (b) OCP curves

Table 1 Corrosion potentials and corrosion current densities of aluminum foil

Reaction system	φ_{corr}(vs Hg/HgO)/V	J_{corr}/(mA·cm^{-2})
NaOH	−1.377	13.56
KOH	−1.359	17.54
TMG	−1.431	10.87
TMAH	−1.461	4.82

This indicates that the TMAH system has the slowest reaction on the aluminum surface and the slowest hydrogen production rate in the Al−H_2O reaction. The corrosion potential (φ_{corr}) of the aluminum foil in the TMAH system (−1.461 V (vs Hg/HgO)) is more negative than that in the KOH system (−1.359 V (vs Hg/HgO)), while the corrosion current density (J_{corr}) in the KOH system is 17.54 mA/cm^2. The pH values in NaOH and KOH solutions are higher than those in TMG and TMAH solutions, so the OH^- concentrations in the solutions are higher under the same molar ratio. Therefore, the corrosion rates of aluminum surfaces in the TMAH and TMG systems are relatively slower.

Figure 3(b) shows that the initial values of OCP for the aluminum foil in the NaOH, KOH, TMG, and TMAH systems were −1.573, −1.567, −1.502, and −1.556 V (vs Hg/HgO), and then positively shifted to a stable potential at −1.400, −1.407, −1.368, and −1.446 V (vs Hg/HgO), respectively. The positive shift of the potential is caused by the formation of the $Al(OH)_3$ layer on the aluminum surface, and the potential is stable when the formation of $Al(OH)_3$ layer and the dissolution of the aluminum foil are in equilibrium [47]. Therefore, the relative potentials of the $Al(OH)_3$ layer in these systems reach equilibrium after 50 min.

The reaction is the fastest in the KOH system and the slowest in the TMAH system, which is consistent with the observation of FBR. This suggests that the catalysts in these systems differ in the reaction potential energy acting on the aluminum surface, which affects the growth pattern of $Al(OH)_3$.

In short, the effect of the catalyst acting on the aluminum surface vanishes as bubbles disappear, implying the reaction of aluminum with water is over.

3.3 Morphology of precipitates

The morphology of the products at different reaction stages was analyzed using TEM, to unravel how it evolves as the reaction progresses. Figure 4(a) shows the evolution of the product morphology with time in the NaOH system. Column-like and irregular particles were observed at 30 min, indicating that the aluminum particles underwent incomplete reactions. The column-like particles were further enlarged at 62 min, but some irregular particles were still present, indicating that crystal growth was incomplete. There were more hexagonal prism particles at 75 min, and the length reached 0.6 μm. The system reached a stable state at 103 min, while most of the particles in the system were hexagonal prismatic and had a length of 0.7 μm. The evolution process of the product in the KOH system is demonstrated in Fig. 4(b). Initially, after 30 min of the reaction, most of the particles were irregular and flocculent, with the incomplete reaction of many aluminum particles. Columnar particles were formed at 51 min, while more hexagonal prism particles were formed at 71 min. However, irregular flocculent particles still remained and the length reached 0.7 μm. The length at 100 min was larger than that at 71 min, reaching 1.2 μm, indicating further growth of the particles. There were irregular flocculent particles enriched in the TMG reaction system at 30 min (Fig. 4(c)). At 69 min, more rod-like particles with flocs were observed, suggesting that the reaction was incomplete. This was followed by an increase in the number of needle-like particles with a length of 2.3 μm at 81 min. At 108 min, the products turned into fine rods and the particles grew up with a length of 5.1 μm. In Fig. 4(d), it can be seen that there were more flocculated particles in the TMAH reaction system at both 30 and 73 min. More rod-shaped particles were generated at 87 min, with a length of 2.8 μm, and the particles were mainly in the form of rods at 98 min, with a length of 3.0 μm.

In general, the Al−H_2O reaction involves the formation of irregular-shaped aluminum hydrate particles, followed by the gradual growth of aluminum hydroxide crystals.

To compare the morphology of the products in each system, the precipitates after 120 min reaction were measured by SEM and TEM. Figures 5 and 6 show the morphologies of the precipitates prepared by each system. The NaOH system generated

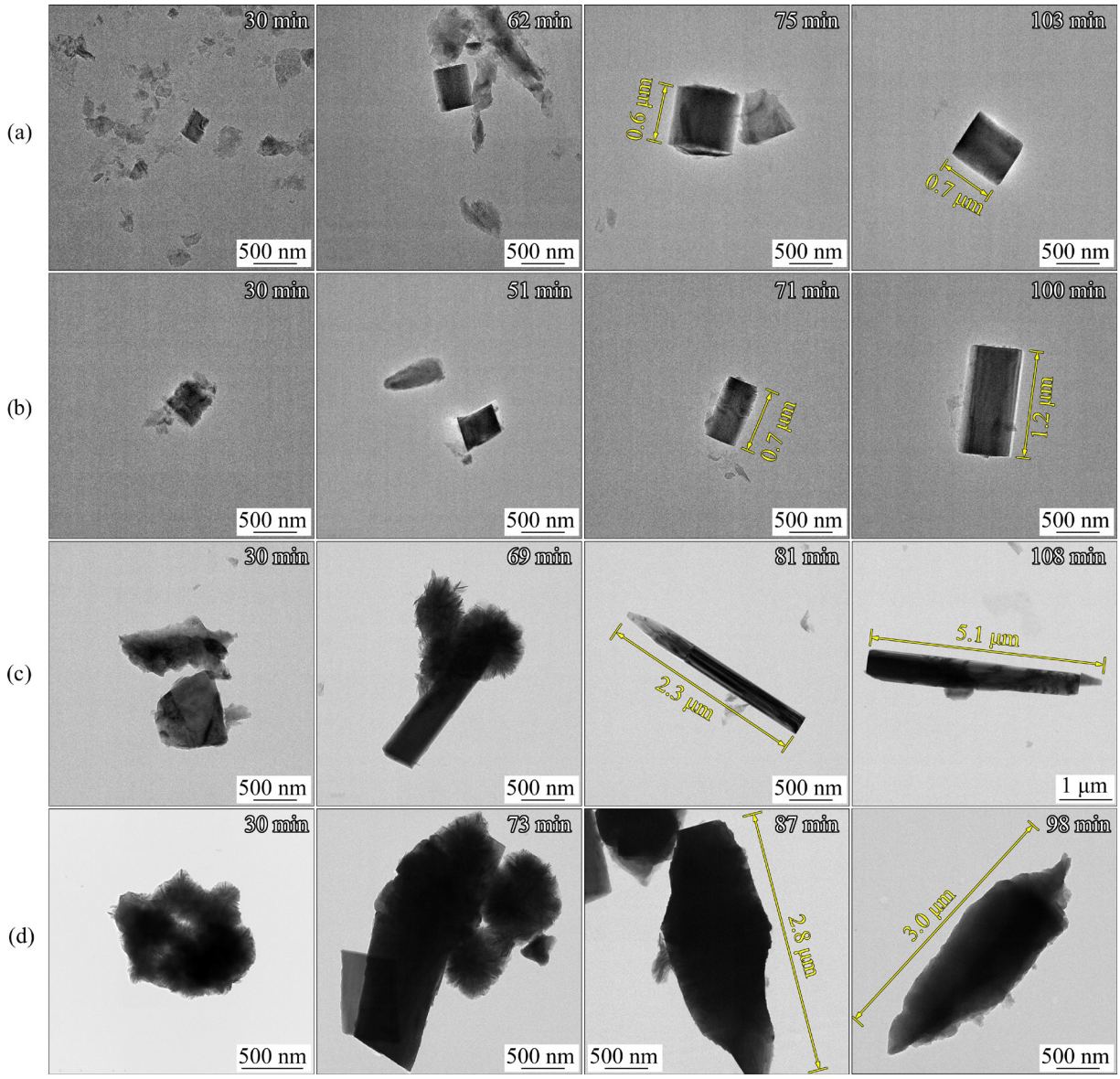

Fig. 4 TEM images of precipitates obtained at different moments in systems of NaOH (a), KOH (b), TMG (c), and TMAH (d)

stacked and aggregated precipitates in block form, with hexagonal prism particles, as shown in Figs. 5(a) and 6(a). The KOH system produced regular prisms, as seen in Fig. 5(b), with long-hexagonal prism particles, as displayed in Fig. 6(b). For the TMG system shown in Fig. 5(c), the precipitates were bar-shaped particles with a stacked form, while the particles in Fig. 6(c) were round bar-shaped. The precipitates obtained from the TMAH system, demonstrated in Fig. 5(d), mainly consisted of a series of bar-like particles in chaos, with irregularly bar-shaped particles, as seen in Fig. 6(d). Thus, it is necessary to conduct a detailed study on the crystal growth mechanisms for a better understanding of these differences in precipitate morphologies.

3.4 Phase and crystal growth habit

An XRD analysis of the products obtained at different time was performed to investigate the difference in the phases. Figure 7(a) shows that the product in the NaOH system is bayerite at 30 min, while it transforms to gibbsite at 62 min. The products at 75 and 103 min are gibbsite and remain as time increases. Bayerite and gibbsite are both of layered structures, where the cohesion between the layers is mainly attributed to hydrogen bonding. Regarding stability, gibbsite is more stable than

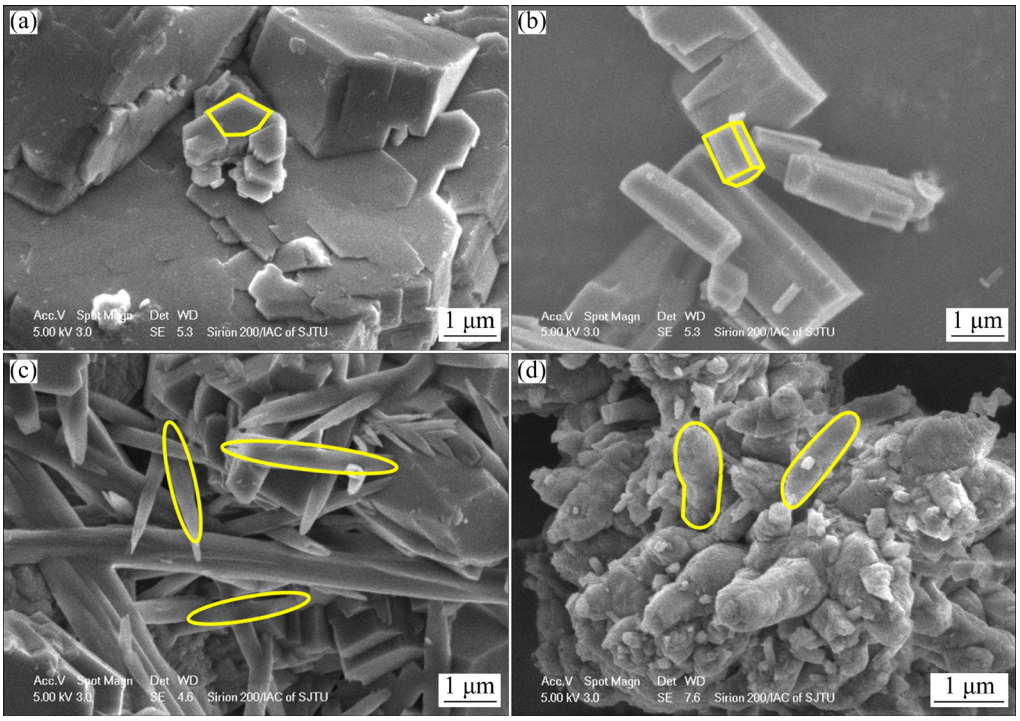

Fig. 5 SEM morphologies of precipitates obtained from reaction of different systems after 120 min: (a) NaOH; (b) KOH; (c) TMG; (d) TMAH

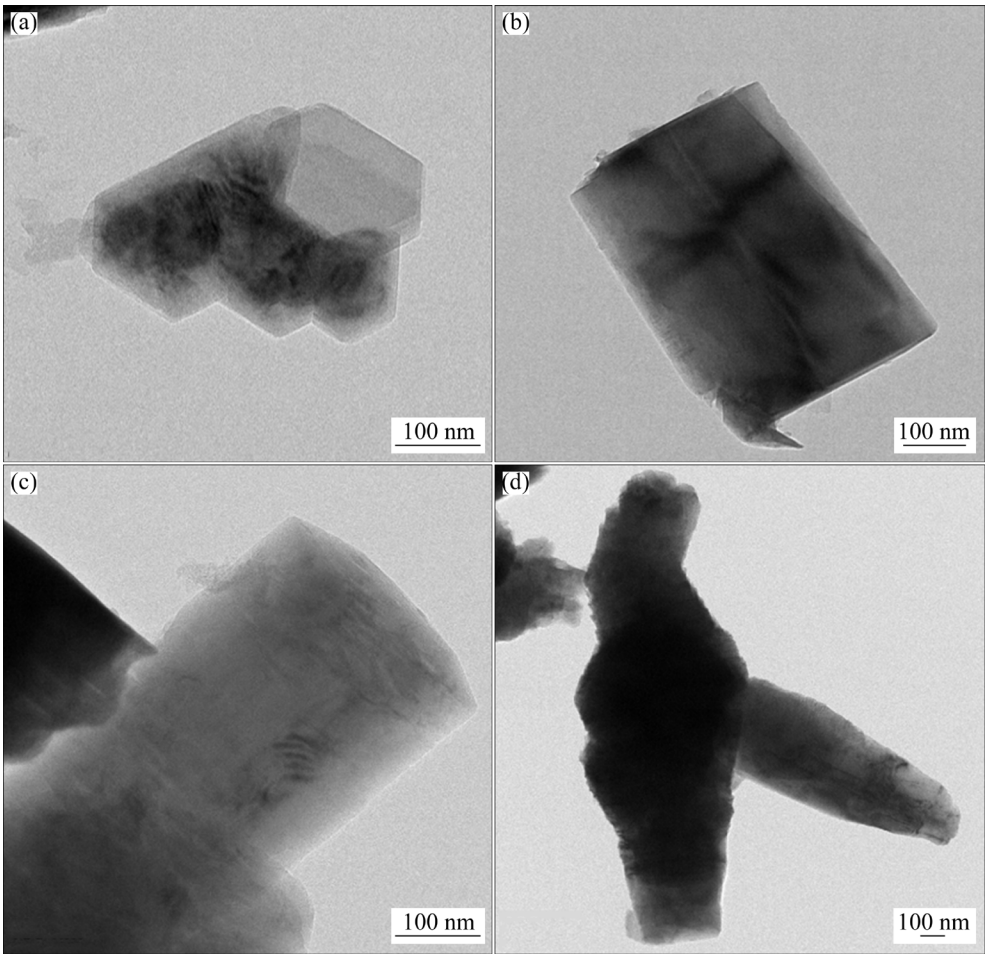

Fig. 6 TEM images of precipitates after 120 min obtained from NaOH (a), KOH (b), TMG (c), and TMAH (d) systems

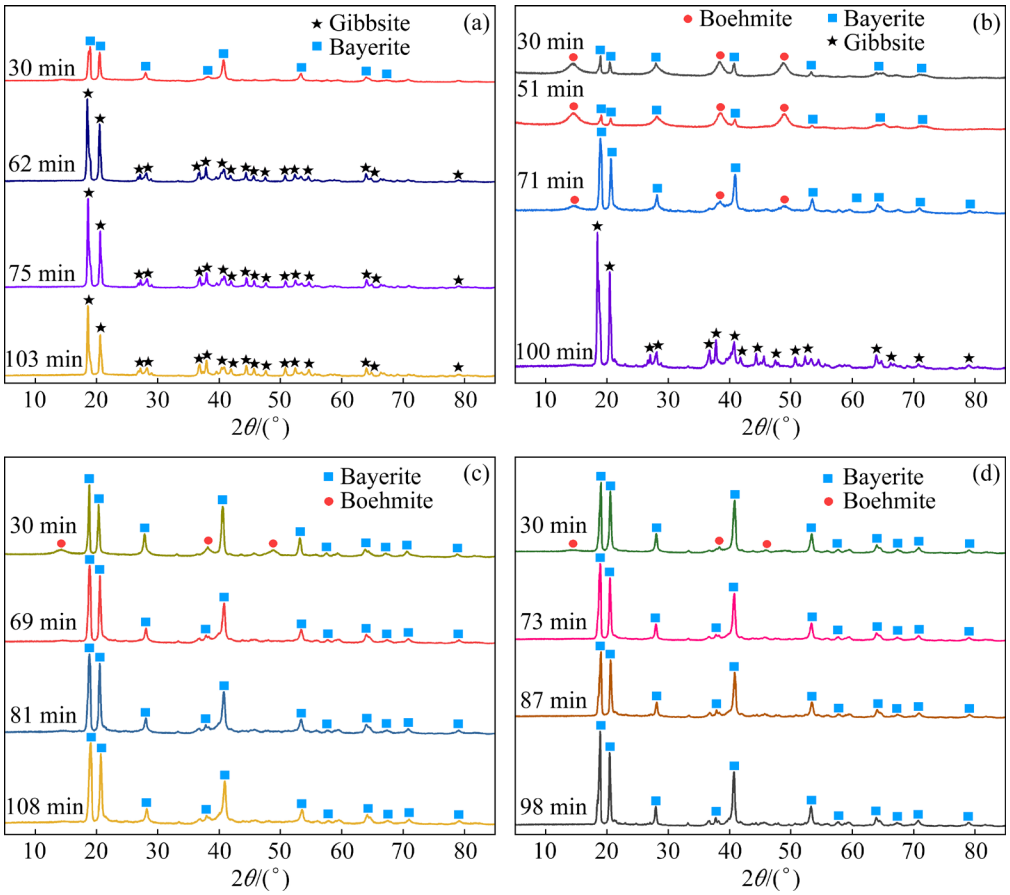

Fig. 7 XRD patterns of precipitates obtained from NaOH (a), KOH (b), TMG (c), and TMAH (d) systems at different moments

bayerite by approximately 8 kJ/mol [48]. Therefore, the environment in the system can change its layers as the reaction progresses, inducing the transformation to relatively more stable gibbsite. Figure 7(b) shows that the phases of the products at 30, 51, and 71 min in the KOH system are bayerite and boehmite, which is attributed to the induction period that occurs on the surface of the Al particles, and the Al—O bonds being converted to Al—OH. Subsequently, the hydrated alumina film is formed and grows rapidly, generating boehmite (AlOOH) on the aluminum surface [49]. Boehmite gradually converts to $Al(OH)_3$ as the reaction progresses, and the KOH system also induces the conversion of bayerite to a relatively stable gibbsite at 100 min.

The phases at 30 min in the TMG (Fig. 7(c)) and TMAH (Fig. 7(d)) systems are bayerite and boehmite, implying that boehmite is also produced during the reaction. The peaks of the products in the two systems are similar after 30 min, and the phases at 108 and 98 min are both bayerite, suggesting that bayerite does not change to other phases in these two systems.

The emergence of boehmite during the initial reaction of Al−H_2O is consistent with the growth patterns of the aluminum particle [49]. The environment in the KOH and NaOH systems can induce bayerite to transform into a relatively more stable gibbsite, but no such environment exists in the TMG and TMAH systems. And this difference could be attributed to the presence of K^+ and Na^+ in the systems [50].

Further characterizations were conducted to elucidate the growth mechanism. The difference in the morphology of the precipitates after 120 min may be associated with different phases. Figure 8 indicates that the peak of the precipitates obtained from the NaOH and KOH systems is consistent with gibbsite (JCPDS: 70-2038), while that from the TMG and TMAH system is consistent with bayerite (JCPDS: 74-1119). And the preferential orientation coefficients (T) are calculated by the XRD spectrum to analyze the growth mechanism of gibbsite and bayerite, as shown in Fig. 9.

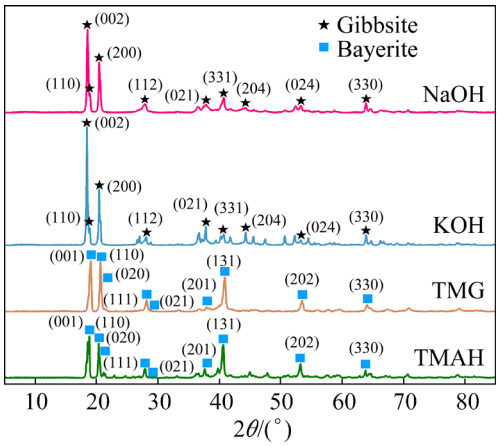

Fig. 8 XRD patterns of precipitates obtained from NaOH, KOH, TMG, and TMAH systems after 120 min

In general, the slower-growing crystal faces become the exposed ones as the crystal face with the preferential growth disappears [46]. The disappearance of the preferentially growing (110) face is promoted by the larger values of T_{110} and T_{330} in NaOH system (Fig. 9(a)). Once the (110) face disappears, the (001) and (100) faces promote the transformation of quadrangular to hexagonal rhombic. Similarly, the preferential growth of the (204) and (024) faces leads to the formation of hexagonal gibbsite crystals with irregular surface features in the NaOH system.

In contrast, much larger value of T_{200} promotes preferential growth on the (100) face in the KOH system, and long-prismatic particles appear when the (100) face disappears. The value of T_{204} and T_{330} is smaller than that of T_{200} and promotes preferential growth of the (204) and (330) faces, determining the growth of the side crystal faces of the gibbsite and promoting the formation of prismatic crystals. Ultimately, the rapid growth on the (100) face in KOH system results in a long-hexagonal prism particle. Notably, the values of T_{204} and T_{112} in the KOH system are larger than those in the NaOH system, and the values of T_{002} and T_{110} in the KOH system are less than those in the NaOH system. The

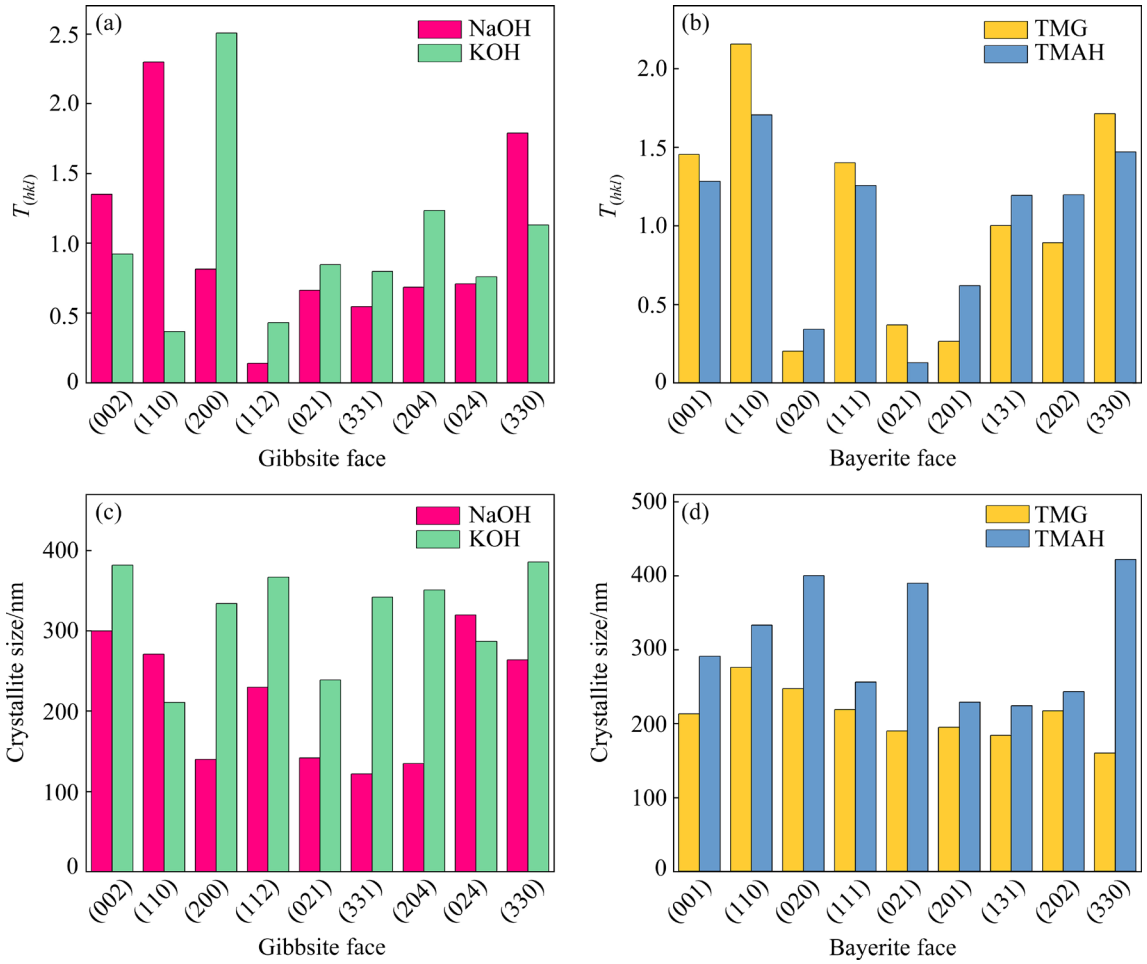

Fig. 9 Preferential orientation coefficients (T) for different faces of gibbsite (a) and bayerite (b), and crystallite sizes of gibbsite (c) and bayerite (d)

difference between the values of T is one of the significant factors affecting particle morphology even though both of them have the same phase. Moreover, a common growth model in the gibbsite crystal growth is a hexagon surrounded by (002), (110), (200), (101), (112), and (11$\bar{2}$) faces [51,52].

Each form of bayerite consists of different proportions of the basal (001) face and the side (111), (110) faces, and most of the bayerite is fine rod-shaped or cone-shaped microcrystals [53]. Figure 9(b) shows that T_{001}, T_{110}, T_{330}, and T_{111} values are relatively large in the TMG and TMAH systems, suggesting they align with the crystal growth mode with bayerite as the basic structure. Therefore, the (110) and (111) faces of the bayerite crystal in the TMG system disappear in advance, and a long bar-shaped structure is formed in the crystal with the exposure of the (020) and (201) faces. In contrast, the T_{111} and T_{110} values are relatively small in the TMAH system, resulting in the slow growth and incomplete disappearance of the side (111) and (110) faces after the reaction to retain the bar structure. Moreover, the T_{131}, T_{202}, and T_{201} values in the TMAH system are larger than those in the TMG system, contributing to the generation of small irregular particles adhering to the surface of bar-shaped crystals in the TMAH system.

Figure 9(c) shows the crystallite sizes corresponding to the different crystal faces, where the (024) face and the (331) face have the largest and the smallest crystallite sizes in the NaOH system, which are 320 and 122 nm, respectively. The largest and smallest crystallite sizes in the KOH system correspond to the (330) face and the (110) face, which are 386 and 211 nm, respectively. The crystallite sizes of the corresponding crystal faces in the NaOH system are generally smaller than those in the KOH system, revealing that the growth of the corresponding crystal face in the NaOH system is significantly slower than that in the KOH system. The crystallite sizes of bayerite crystals in the TMG system are smaller than those in the TMAH system, and the largest value of both is in the (110) face and the (330) face, reaching 276 and 422 nm, respectively. On the contrary, the smallest value is in the (330) face and (131) face, reaching 160 and 224 nm, respectively (Fig. 9(d)). The crystal growth of the corresponding crystal face in the TMAH system is faster.

Therefore, the difference in crystallite size is also one of the reasons for the difference in crystal morphology, which explains why the particle morphology shows differences in solutions at the same moment during the observation of FBR. This implies that there is no relationship between the preferential growth face and the crystallite size during the growth of $Al(OH)_3$ crystal.

3.5 Properties of precipitates

Figure 10(a) displays the diffraction spots of the product obtained in the NaOH system, which was marked at the axis of [001] for the (110) and (200) faces, and the lattice fringe of the (200) faces could be found in the HRTEM image. Similarly, the products in the KOH system (Fig. 10(b)) were marked at the axis of [010] for the (200), (204) and (002) diffraction spots, and the lattice stripe corresponded to the (200) face. The products in the TMG system (Fig. 10(c)) have the (111) and (110) faces corresponding to the [1$\bar{1}$0] axis, and the lattice stripe in the HRTEM image corresponded to the (110) face. Figure 10(d) shows that the diffraction spots corresponding to the TMAH system in the [010] axis have the (202), (201), and (001) faces, while the lattice stripe in the HRTEM image corresponded to the (202) face. The analysis by SAED and HRTEM reveals that the exposed face in these systems is consistent with the XRD analysis. Therefore, the growth trend of the crystal faces is the main factor that causes the difference in the morphology of these products.

The FTIR spectra of the products in different systems were obtained. The peaks within 3400−3700 cm^{-1} are related to the asymmetric stretching vibrations of hydroxyl, and the peaks at 500−1000 cm^{-1} are related to the Al—O bond [43]. Figure 11(a) shows that the peaks of the products at different moments in the NaOH system are mainly free water (1639 and 1328 cm^{-1}), —OH bond, and Al—O bond [54]. The Al—O bonds at 30 and 62 min were relatively less, while the content of Al—O bond gradually increased as the reaction proceeded. The peak for the free water at 1328 cm^{-1} disappeared at 103 min, implying that the crystals tended to be more stable. Figure 11(b) suggests that the products from the KOH system contained (Al)O—H bonds of boehmite at 30, 51, and 71 min (at 2975 cm^{-1}) [55], and the Al—O bonds of the product were relatively less at the beginning of the

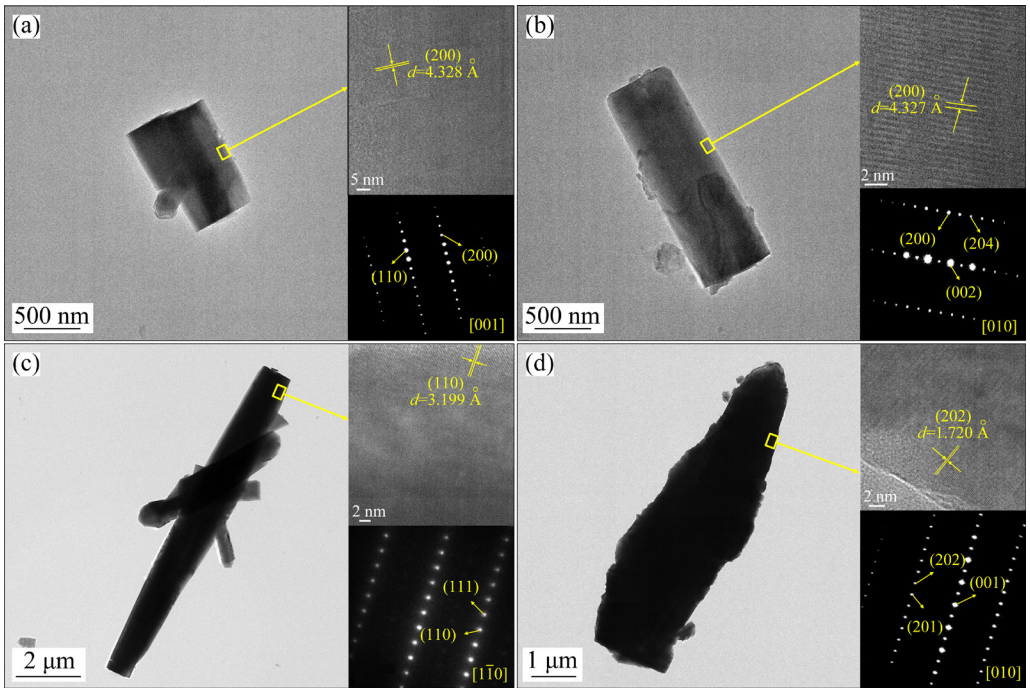

Fig. 10 TEM image, HR-TEM image, and SAED pattern of products obtained from NaOH (a), KOH (b), TMG (c), and TMAH (d) systems after 120 min

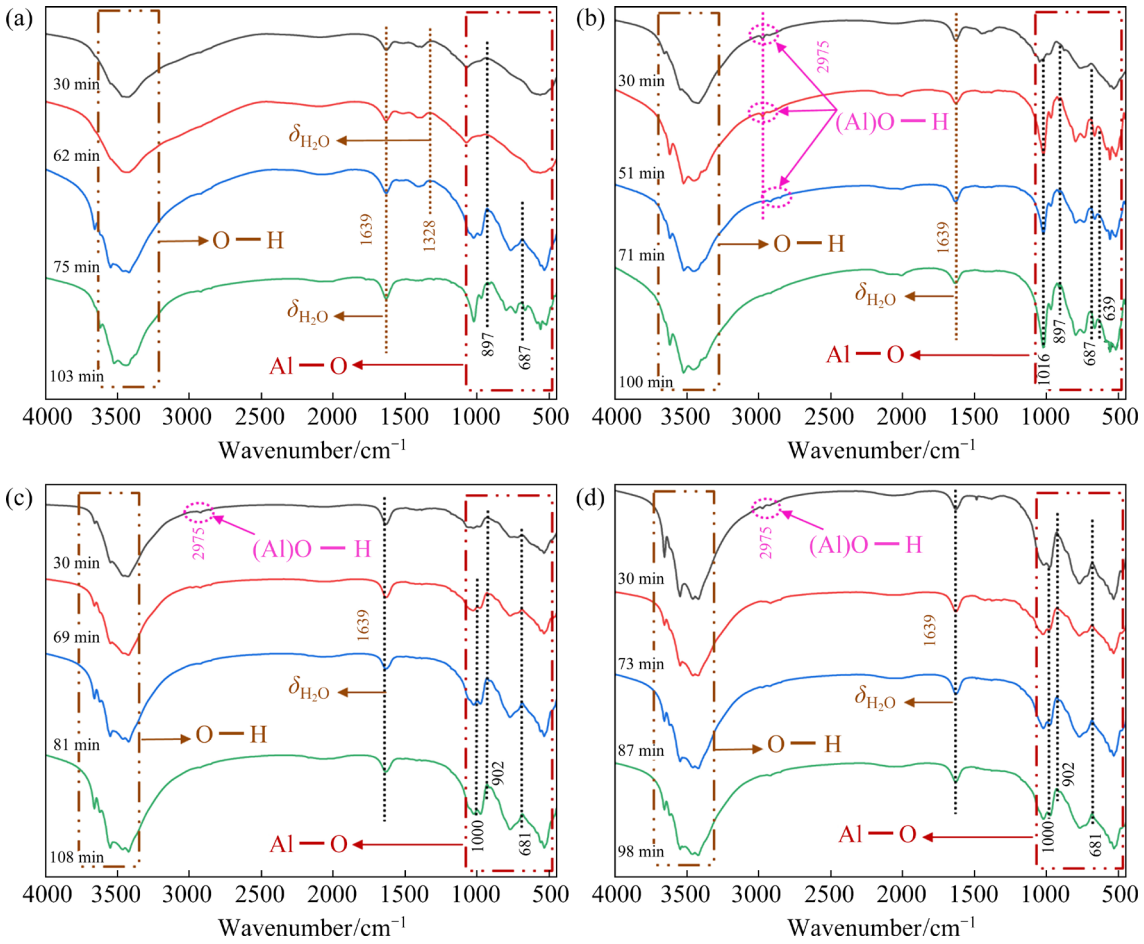

Fig. 11 FTIR spectra of products obtained from NaOH (a), KOH (b), TMG (c), and TMAH (d) systems at different moments

reaction (30 min), while there were more Al—O bonds after 51 min. The peaks in the TMG and TMAH systems were similar (Figs. 11(c, d)), and both had the (Al)O—H bond (2975 cm^{-1}) of boehmite at 30 min. The Al—O bonds of the products in both systems changed less after 30 min. Notably, the products in all four systems produce a δ_{H_2O} (free water) peak at 1639 cm^{-1}, which is related to the structure of $Al(OH)_3$. Moreover, the Al—O bonds of products in the TMG and TMAH systems are less than those in the NaOH and KOH systems. The (Al)O—H bond indicates the presence of boehmite in the products, which is consistent with the phase analysis results.

Subsequently, the FTIR spectra of these precipitates after 120 min were analyzed to compare their differences. Figure 12 shows that peaks around the absorption band of 3620, 3530, and 3420 cm^{-1} were related to the asymmetric stretching vibrations of hydroxyl, and the peaks at 500−1000 cm^{-1} were related to the Al—O bond [56]. The bands centered at 542, 639, and 687 cm^{-1} were asymmetric bending vibrations of Al—O bonds of precipitates in the NaOH and KOH systems, while the TMG and TMAH systems had only one asymmetric bending vibration of Al—O bonds at 681 cm^{-1}. This explains that gibbsite and bayerite have very similar in-plane lattice structures, and both of them consist of the same single-layer component ($Al(OH)_3$), but the different stacking order results in different hydrogen bonding configurations [57]. This leads to the peaks of Al—O bonds having different absorption bands in gibbsite and bayerite. In particular, the Al—O bonds of $Al(OH)_3$ at 500−1000 cm^{-1} promote the

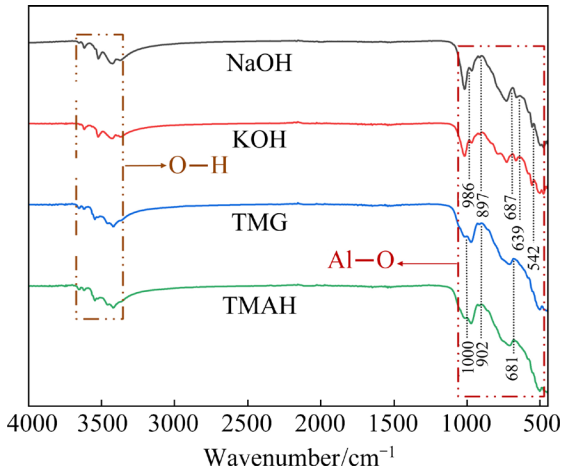

Fig. 12 FTIR spectra of products after 120 min

composition of the columnar crystal. The differences in $Al(OH)_3$ crystal structure obtained in these systems also result in different morphologies.

The growth mechanism of $Al(OH)_3$ prepared with these four catalysts is proposed in Fig. 13. The oxide film on the aluminum is first destroyed and removed by the alkaline catalyst, and then the reaction of aluminum with water leads to the formation of $Al(OH)_3$ and hydrogen gas. It has been observed that the growth trends of each crystal face of $Al(OH)_3$ are distinct under these conditions. The preferential growth face of the gibbsite is (110) (NaOH) and (100) (KOH). Similarly, the preferential growth face of bayerite is (110) (TMG and TMAH). Other faces exhibit different growth trends that can influence the morphology of $Al(OH)_3$.

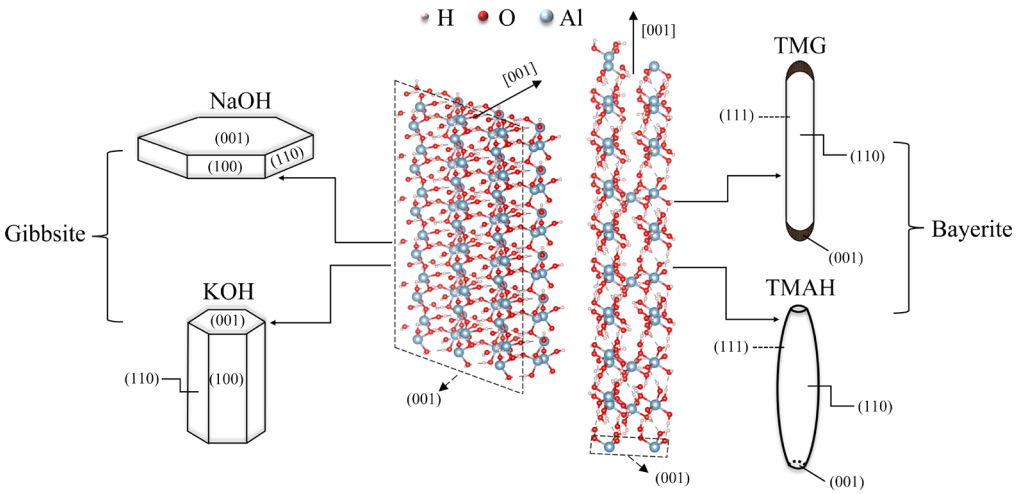

Fig. 13 Schematic diagram of morphological evolution mechanisms of gibbsite and bayerite

4 Conclusions

(1) The Al−H_2O reaction was carried out at a molar ratio of 1:2 of catalyst (NaOH, KOH, TMG, and TMAH) to aluminum powder at 85 °C. And the disappearance of bubbles in the solution observed in situ occurred at 62, 51, 69, and 73 min, respectively. The KOH system has the largest reaction rate in hydrogen production and the highest corrosion current density on the aluminum surface, revealing the highest reaction potential energy acting on the aluminum surface. The precipitates after 120 min exhibit hexagonal prisms, long-hexagonal prisms, long rods, and irregular rods, respectively.

(2) The reaction products are bayerite or gibbsite. It is suggested that $Al(OH)_3$ grows along with the (110), (001), and (100) faces in the NaOH system, and the (100), (102), and (110) faces in the KOH system. The differences in the morphology of the gibbsite are caused by the different exposure patterns of the other faces. The $Al(OH)_3$ crystals in both TMG and TMAH systems grow along the (110), (111), and (001) faces, and the generation of irregularly-shaped particles in the TMAH system is attributed to the preferential growth of the (131), (202), and (201) faces. The exposed crystal faces are confirmed by the HR-TEM image and SAED pattern.

(3) The larger crystallite size indicates faster crystal growth of the corresponding crystal face, and the gibbsite in the KOH systems and bayerite in the TMAH systems have a larger growth rate on some crystal faces. The gibbsite has more peaks of Al—O bonds than the bayerite at 500−1000 cm^{-1}, promoting the production of columnar crystals.

CRediT authorship contribution statement

Wen-qi TANG：Investigation, Writing − Original draft; **Ji-yi ZHU:** Resources, Formal analysis; **Hui SUN:** Formal analysis; **Yong-fei JUAN:** Characterization; **Chao-peng FU:** Writing − Review & editing, Supervision; **Jian YANG:** Formal analysis, Conceptualization; **Jiao ZHANG:** Conceptualization, Supervision.

Declaration of competing interest

The authors declare that they have no known competing financial interests or personal relationships that could have appeared to influence the work reported in this paper.

Acknowledgments

This work was supported by the National Natural Science Foundation of China (No. 51627802) and the Inner Mongolia Science and Technology Revitalization Project, China (No. XM2020BT14).

References

[1] ZHU Xing-kun, ZOU Nan, PANG Hong-chang, TIAN Peng, NING Gui-ling. Fabrication of hierarchical core−shell $AlPO_4$@$Al(OH)_3$ with high flame-retardant performance [J]. Chemical Physics Letters, 2020, 759: 137943. DOI: 10.1016/j.cplett.2020.137943

[2] YUSUF M O, JOHARI M, AHMAD Z A, MASLEHUDDIN M. Effects of addition of $Al(OH)_3$ on the strength of alkaline activated ground blast furnace slag-ultrafine palm oil fuel ash (AAGU) based binder [J]. Construction & Building Materials, 2014, 50(15): 361−367. DOI: 10.1016/j.conbuildmat.2013.09.054

[3] GUERRERO-FLORES Á D, ELIZONDO-ÁLVAREZ M A, FLORES-ÁLVAREZ J M, URIBE-SALAS A. Comparative study on simultaneous removal of calcium and sulfate ions from flotation recycling water by aluminum hydroxide [J]. Transactions of Nonferrous Metals Society of China, 2022, 32(7): 2379−2390. DOI: 10.1016/S1003-6326(22)65954-5

[4] BELLA M L, HAMIDOUCHE M, GREMILLARD L. Preparation of mullite−alumina composite by reaction sintering between Algerian kaolin and amorphous aluminum hydroxide [J]. Ceramics International, 2021, 47(2): 16208−16220. DOI: 10.1016/j.ceramint.2021.02.199

[5] HE Y J, MA B. Molecular dynamics analysis on bending mechanical behavior of alumina nanowires at different loading rates [J]. Transactions of Nonferrous Metals Society of China, 2022, 32(11): 3687−3698. DOI: 10.1016/S1003-6326(22)66049-7

[6] NALIVAIKO A Y, OZHERELKOV D Y, PAK V I, KIROV S S, GROMOV A A. Preparation of aluminum hydroxide during the synthesis of high purity alumina via aluminum anodic oxidation [J]. Metallurgical and Materials Transactions B, 2020, 51(7): 1154−1161. DOI: 10.1007/s11663-020-01829-5

[7] SMITH P, POWER G. High purity alumina–Current and future production [J]. Mineral Processing and Extractive Metallurgy Review, 2021, 43(6): 747−756. DOI: 10.1080/08827508.2021.1937150

[8] ANTHONY N, K. RAVINDRANATHAN T. Novel amorphous aluminum hydroxide catalysts for aluminum–water reactions to produce H_2 on demand [J]. International Journal of Hydrogen Energy, 2017, 42(37): 23446−23454. DOI: 10.1016/j.ijhydene.2017.04.279

[9] WANG Hong-qi, WANG Zhi, GUO Jian-wei, SHI Zhi-hao, GONG Xu-zhong, CAO Jian-wei. Boehmite preparation via alditols-interacting transformation of metastable intermediates in Al−H_2O reaction crystallization [J]. Crystal

Growth & Design, 2017, 17(1): 183−190. DOI: 10.1021/acs.cgd.6b01408

[10] ALINEJAD B, MAHMOODI K. A novel method for generating hydrogen by hydrolysis of highly activated aluminum nanoparticles in pure water [J]. International Journal of Hydrogen Energy, 2009, 34(19): 7934−7938.

[11] DENG Z, FERREIRA J, TANAKA Y, YE J. Physicochemical mechanism for the continuous reaction of γ-Al_2O_3-modified aluminum powder with water [J]. Journal of the American Ceramic Society, 2007, 90(5): 1521−1526. DOI: 10.1111/j.1551-2916.2007.01546.x

[12] DENG Z Y, ZHU L L, TANG Y B, SAKKA Y, XIE R J. Role of particle sizes in hydrogen generation by the reaction of Al with water [J]. Journal of the American Ceramic Society, 2010, 93(10): 2998−3001. DOI: 10.1111/j.1551-2916.2010.03969.x

[13] ZHANG H, ZHANG X, GRAHAM T R, PEARCE C I, ROSSO K M. Crystallization and phase transformations of aluminum (Oxy) hydroxide polymorphs in caustic aqueous solution [J]. Inorganic Chemistry, 2021, 60(13): 9820−9832. DOI: 10.1021/acs.inorgchem.1c01111

[14] OH Y H, CHANG K R, KIM D H, LEE G H, KIM W W. Formation characteristics of an aluminum hydroxide fiber by a hydrolysis of aluminum nano powder [J]. Journal of Materials Science, 2006, 41(13): 4191−4195. DOI: 10.1007/s10853-006-6988-7

[15] PANCHAKARLA L S, SHAH M A, GOVINDARAJ A, RAO C. A simple method to prepare ZnO and $Al(OH)_3$ nanorods by the reaction of the metals with liquid water [J]. Journal of Solid State Chemistry, 2007, 180(11): 3106−3110. DOI: 10.1016/j.jssc.2007.09.005

[16] MAHMOODI K, ALINEJAD B. Fast and facile synthesis of boehmite nanofibers [J]. Powder Technology, 2010, 199(3): 289−292. DOI: 10.1016/j.powtec.2010.01.019

[17] THIRUCHITRAMBALAM M, PALKAR V R, GOPINATHAN V. Hydrolysis of aluminium metal and sol−gel processing of nano alumina [J]. Materials Letters, 2004, 58(24): 3063−3066. DOI: 10.1016/j.matlet.2004.05.043

[18] VOSTRIKOV A A, FEDYAEVA O N. Mechanism and kinetics of Al_2O_3 nanoparticles formation by reaction of bulk Al with H_2O and CO_2 at sub- and supercritical conditions [J]. The Journal of Supercritical Fluids, 2010, 55(1): 307−315. DOI: 10.1016/j.supflu.2010.05.022

[19] ZHANG J, KLASKY M, LETELLIER B C. The aluminum chemistry and corrosion in alkaline solutions [J]. Journal of Nuclear Materials, 2009, 384(2): 175−189. DOI: 10.1016/j.jnucmat.2008.11.009

[20] RAZAVI-TOUSI S S, NEMATOLLAHI G A, EBADZADEH T, SZPUNAR, J A. Modifying aluminum–water reaction to generate nano-sized aluminum hydroxide particles beside hydrogen [J]. Powder Technology, 2013, 241: 166−173. DOI: 10.1016/j.powtec.2013.03.025

[21] LLOYD S, THURGATE S M, CORNELL R M, PARKINSON G M. Atomic force microscopy of gibbsite [J]. Applied Surface Science, 1998, 135(1/2/3/4): 178−182. DOI: 10.1016/S0169-4332(98)00283-9

[22] SWEEGERS C, BOERRIGTER S, GRIMBERGEN R, MEEKES H, FLEMING S, HIRALAL I, RIJKEBOER A. Morphology prediction of gibbsite crystals an explanation for the lozenge-shaped growth morphology [J]. Journal of Physical Chemistry B, 2002, 106(5): 1004−1012. DOI: 10.1021/jp0120054

[23] HUANG Wen-qiang, LIU Gui-hua, JU Jin-bin, LI Xiao-bin, ZHOU Qiu-sheng, QI Tian-gui, PENG Zhi-hong. Effect of lithium ion on seed precipitation from sodium aluminate solution [J]. Transactions of Nonferrous Metals Society of China, 2019, 29(6): 1323−1331. DOI: 10.1016/S1003-6326(19)65039-9

[24] LIU Gui-hua, LI Zheng, LI Xiao-bin, QI Tian-gui, PENG Zhi-hong, ZHOU Qiu-sheng. Precipitation of spherical boehmite from concentrated sodium aluminate solution by adding gibbsite as seed [J]. International Journal of Minerals, Metallurgy and Materials, 2017, 24(8): 954−963. DOI: 10.1007/s12613-017-1483-5

[25] WANG S, ZHANG X, GRAHAM T R, ZHANG H, PEARCE C I, WANG Z, CLARK S B, JIANG W, ROSSO K M. Two-step route to size and shape controlled gibbsite nanoplates and the crystal growth mechanism [J]. CrystEngComm, 2020, 22: 2555−2565. DOI: 10.1039/D0CE00114G

[26] SWEEGERS C, CONINCK H, MEEKES H, ENCKEVORT W, RIJKEBOER A. Morphology, evolution and other characteristics of gibbsite crystals grown from pure and impure aqueous sodium aluminate solutions [J]. Journal of Crystal Growth, 2001, 233(3): 567−582. DOI: 10.1016/S0022-0248(01)01615-3

[27] KOGA N, TANAKA T F. Preparation and thermal decomposition of synthetic bayerite [J]. Journal of Thermal Analysis & Calorimetry, 2001, 64: 965−972. DOI: 10.1023/A:1011531215596

[28] WEI Guang-ye, QU Jing-kui, ZHENG Yu-dong, QI Tao, GUO Qiang, HAN Bing-bing, ZHAO Hong-xin. Crystallization behaviors of bayerite from sodium chromate alkali solutions [J]. Transactions of Nonferrous Metals Society of China, 2014, 24(10): 3356−3365. DOI: 10.1016/S1003-6326(14)63477-4

[29] LEFÈVRE G, FéDOROFF M. Synthesis of bayerite (β-$Al(OH)_3$) microrods by neutralization of aluminate ions at constant pH [J]. Materials Letters, 2002, 56(6): 978−983. DOI: 10.1016/S0167-577X(02)00650-X

[30] SHAYANFAR S, AGHAZADEH V, SARAVARI A, HASANPOUR P. Aluminum hydroxide crystallization from aluminate solution using carbon dioxide gas: Effect of temperature and time [J]. Journal of Crystal Growth, 2018, 496/497: 1−9. DOI: 10.1016/j.jcrysgro.2018.04.028

[31] ZOLFAGHARI R, REZAI B, BAHRI Z, MAHMOUDIAN M. Influences of new synthesized active seeds and industrial seed on the aluminum hydroxide precipitation from sodium aluminate solution [J]. Journal of Sustainable Metallurgy, 2020, 6: 643−658. DOI: 10.1007/s40831-020-00302-6

[32] JIAO W Q, YUE M B, WANG Y M, HE M Y. Synthesis of morphology-controlled mesoporous transition aluminas derived from the decomposition of alumina hydrates [J]. Microporous and Mesoporous Materials, 2012, 147(1): 167−177. DOI: 10.1016/j.micromeso.2011.06.012

[33] LEFÈVRE G, PICHOT V, FÉDOROFF M. Controlling particle morphology during growth of bayerite in aluminate solutions [J]. Chemistry of Materials, 2003, 15(13):

2584−2592. DOI: 10.1021/cm0310059

[34] ALEKSANDROV Y A, TSYGANOVA E I, PISAREV A L. Reaction of aluminum with dilute aqueous NaOH solutions [J]. Russian Journal of General Chemistry, 2003, 73(5): 689−694. DOI: 10.1023/A:1026114331597

[35] LI Xiao-bin, YAN Li, ZHOU Qiu-sheng, LIU Gui-hua, PENG Zhi-hong. Thermodynamic model for equilibrium solubility of gibbsite in concentrated NaOH solutions [J]. Transactions of the Nonferrous Metals Society of China, 2012, 22(2): 447−455. DOI: 10.1016/s1003-6326(11)61197-7

[36] YANG B C, CHAI Y J, YANG F L, ZHANG Q, LIU H, WANG N. Hydrogen generation by aluminum−water reaction in acidic and alkaline media and its reaction dynamics [J]. International Journal of Energy Research, 2018, 42(4): 1594−1602. DOI: 10.1002/er.3953

[37] TANG Wen-qi, YAN Li-hong, LI Kai-qi, JUAN Yong-fei, FU Chao-peng, ZHANG Jiao. A comparison study on aluminum-water reaction with different catalysts [J]. Materials Today Communications, 2022, 31: 103517. DOI: 10.1016/j.mtcomm.2022.103517

[38] VERDES G, GOUT R, CASTET S. Thermodynamic properties of the aluminate ion and of bayerite, boehmite, diaspore and gibbsite [J]. European Journal of Mineralogy, 1992, 4(4): 767−792. DOI: 10.1127/ejm/4/4/0767

[39] LI Xiao-bin, WANG Dan-qin, ZHOU Qiu-sheng, LIU Gui-hua, PENG Zhi-hong. Concentration variation of aluminate ions during the seeded precipitation process of gibbsite from sodium aluminate solution [J]. Hydrometallurgy, 2011, 106(1/2): 93−98. DOI: 10.1016/j.hydromet.2010.12.002

[40] SWEEGERS C, MEEKES H, VAN ENCKEVORT W, HIRALAL I, RIJKEBOER A. Growth rate analysis of gibbsite single crystals growing from aqueous sodium aluminate solutions [J]. Crystal Growth & Design, 2004, 4(1): 185−198. DOI:10.1021/cg030004q

[41] KUMARA C K, NG W J, BANDARA A, WEERASOORIYA R. Nanogibbsite: Synthesis and characterization [J]. Journal of Colloid and Interface Science, 2010, 352(2): 252−258. DOI: 10.1016/j.jcis.2010.08.083

[42] LI T S, LIVK I, ILIEVSKI D. Supersaturation and temperature dependency of gibbsite growth in laminar and turbulent flows [J]. Journal of Crystal Growth, 2003, 258(3/4): 409−19. DOI: 10.1016/S0022-0248(03)01557-4

[43] DU Xue-lian, WANG Yan-qin, SU Xing-hua, LI Jian-gong. Influences of pH value on the microstructure and phase transformation of aluminum hydroxide [J]. Powder Technology, 2009, 192(1): 40−46. DOI: 10.1016/j.powtec.2008.11.008

[44] SWEEGERS C, VAN ENCKEVORT W, MEEKES H, BENNEMA P, HIRALAL I, RIJKEBOERA. The impact of twinning on the morphology of γ-$Al(OH)_3$ crystals [J]. Journal of Crystal Growth, 1999, 197(1/2): 244−253. DOI: 10.1016/S0022-0248(98)00899-9

[45] ALVAREZ A J, MYERSON A S. Continuous plug flow crystallization of pharmaceutical compounds [J]. Crystal Growth & Design, 2010, 10(5): 2219−2228. DOI: 10.1021/cg901496s

[46] HUANG Wen-qiang, LIU Gui-hua, QI Tian-gui, LI Xiao-bin, ZHOU Qiu-sheng, PENG Zhi-hong. Effects of pH and ions on the morphological evolution of boehmite prepared by hydrothermal treatment of ultrafine Bayer gibbsite [J]. CrystEngComm, 2020, 22: 6983−6992. DOI: 10.1039/D0CE00808G

[47] REN Jian-ming, LIU Tao, ZHANG Jiao, JIANG Min, DONG Qing, Fu Chao-peng. Spray-formed commercial aluminum alloy anodes with suppressed self-corrosion for Al−air batteries [J]. Journal of Power Sources, 2022, 524: 231082. DOI: 10.1016/j.jpowsour.2022.231082

[48] DEMICHELIS R, CIVALLERI B, NOEL Y, MEYER A, DOVESI R. Structure and stability of aluminium trihydroxides bayerite and gibbsite: A quantum mechanical ab initio study with the $C_{rystal}06$ code [J]. Chemical Physics Letters, 2008, 465(4/5/6): 220−225. DOI: 10.1016/j.cplett.2008.09.070

[49] SACELEANU F, VUONG T V, MASTER E R, WEN J Z. Tunable kinetics of nanoaluminum and microaluminum powders reacting with water to produce hydrogen [J]. International Journal of Energy Research, 2019, 43(13): 7384−7396. DOI: 10.1002/er.4769

[50] PRODROMOU K P, PAVLATOU-VE A S. Formation of aluminum hydroxides as influenced by aluminum salts and bases [J]. Clays and Clay Minerals, 1995, 43(1): 111−115. DOI: 10.1346/CCMN.1995.0430113

[51] FLEMING S, ROHL A, LEE M Y, GALE J, PARKINSON G. Atomistic modelling of gibbsite: Surface structure and morphology [J]. Journal of Crystal Growth, 2000, 209(1): 159−166. DOI: 10.1016/S0022-0248(99)00479-0

[52] CHEN Guo-hui, CHEN Qi-yuan, YIN Zhou-lan, YIN Zhi-min. Characterization of irregular seeds on gibbsites precipitated from caustic aluminate solutions [J]. Transactions of Nonferrous Metals Society of China, 2006, 16(2): 483−487. DOI: 10.1016/S1003-6326(06)60083-6

[53] NAGENDRAN S, KAMATH P V. Synthon approach to structure models for the bayerite-derived layered double hydroxides of Li and Al [J]. Inorganic Chemistry, 2017, 56(9): 5026−5033. DOI: 10.1021/acs.inorgchem.7b00119

[54] KAMARAJ R, VASUDEVAN S. Facile one-pot electro-synthesis of $Al(OH)_3$–kinetics and equilibrium modeling for adsorption of 2,4,5-trichlorophenoxyacetic acid from aqueous solution [J]. New Journal of Chemistry, 2016, 40(3): 2249−2258. DOI: 10.1039/C5NJ02407B

[55] PRIYA G K, PADMAJA P, WARRIER K, DAMODARAN A D, ARULDHAS G. Dehydroxylation and high temperature phase formation in sol-gel boehmite characterized by Fourier transform infrared spectroscopy [J]. Journal of Materials Science Letters, 1997, 16(19): 1584−1587. DOI: 10.1023/A:1018568418302

[56] LIU Xiu-wu, WANG Yu-xing, CUI Xiao-yuan, ZHU Shi-jie, Cao Ji-lin. Fluoride removal from wastewater by natural and modified gibbsite [J]. Journal of Chemical & Engineering Data, 2020, 66(1): 658−668. DOI: 10.1021/ol1009416

[57] KIM D, JUNG J H, IHM J. Theoretical study of aluminum hydroxide as a hydrogen-bonded layered material [J]. Nanomaterials, 2018, 8(6): 375. DOI: 10.3390/nano8060375

Al−H_2O 反应中催化剂对 $Al(OH)_3$ 形貌演化的作用机理

唐文奇[1]，朱基裔[1]，孙 会[2]，隽永飞[1]，付超鹏[1]，杨 健[1]，张 佼[1,3]

1. 上海交通大学 材料科学与工程学院 金属基复合材料国家重点实验室，上海 200240；
2. 上海电机学院 机械学院，上海 201306；
3. 上海交通大学 先进船舶和深海勘探协同创新中心，上海 200240

摘 要：研究不同催化剂在铝−水(Al−H_2O)反应中对 $Al(OH)_3$ 晶体形貌及其生长机理的作用。采用 NaOH、KOH、四甲基胍 (TMG)和四甲基氢氧化铵(TMAH)作为催化剂进行反应，原位观察产物的演化过程。结果表明，反应 120 min 后得到的产物分别具有六棱柱形、六棱长柱状、长棒状和不规则棒状。在 NaOH 和 KOH 体系中，产物为三水铝石，三水铝石在 NaOH 体系中主要沿 (110)、(001)和(100)晶面生长，而在 KOH 体系中主要沿(100)、(102)和(110)晶面生长。在 TMG 和 TMAH 体系中，产物是拜耳石，拜耳石在这两个体系中均沿 (110)、(111)和(001)晶面生长。其中，三水铝石的 Al—O 键较多，有利于柱状晶体的形成。

关键词：晶体生长；氢氧化铝；择优生长因子；铝−水反应；原位观察

(Edited by Bing YANG)